Interface Design for High-Performance All-Solid-State Lithium Batteries

*Hongli Wan, Bao Zhang, Sufu Liu, Zeyi Wang, Jijian Xu, Chunsheng Wang**

H. L. Wan, S. F. Liu, Z. Y. Wang, J. J. Xu, C. S. Wang

Department of Chemical and Biomolecular Engineering, University of Maryland, College Park, MD 20740, USA.

E-mail: cswang@umd.edu (C. S. Wang)

B. Zhang

School of Physical and Mathematical Sciences, Nanyang Technological University, Singapore, 637371, Singapore.

Keywords: mix-conductive interphase, lithiophobic/lithophilic interlayer, lithium dendrite suppression, coulombic efficiency, all-solid-state lithium-metal battery

All-solid-state batteries suffer from high interface resistance and lithium dendrite growth leading to low Li plating/stripping Coulombic efficiency (CE) of <90% and low critical current density at high capacity. Here, we simultaneously address both challenges and significantly increase the Li plating/stripping CE to 99.6% at 0.2 mA cm^{-2}/0.2 mAh cm^{-2}, and CCD of > 3.0 mA cm^{-2}/3.0 mAh cm^{-2} by inserting a mixed ionic-electronic conductive (MIEC) & lithiophobic LiF-C-Li_3N-Bi nanocomposite interlayer between Li_6PS_5Cl electrolyte and Li anode. The highly lithiophobic LiF-C-Li_3N-Bi interlayer with high ionic conductivity (10^{-5} S cm^{-1}) and low electronic conductivity (3.4×10^{-7} S cm^{-1}) enables Li to plate on the current collector (CC) surface rather than on Li_6PS_5Cl surface avoiding Li_6PS_5Cl electrolyte reduction. During initial Li plating on CC, Li penetrates into porous LiF-C-Li_3N-Bi interlayer and lithiates Bi nanoparticles into Li_3Bi. The lithiophilic Li_3Bi and Li_3N nanoparticles in LiF-C-Li_3N-Li_3Bi sub-interlayer will move to CC along with plated Li, forming LiF-C/Li_3N-Li_3Bi lithiophobic/lithiophilic sublayer during the following Li stripping. This interlayer enables $Co_{0.1}Fe_{0.9}S_2$/Li_6PS_5Cl/Li cell with an areal capacity of 1.4 mAh cm^{-2} to achieve a cycle life of >850 cycles at 150 mA g^{-1}. The lithiophobic/lithiophilic interlayer enables solid-state metal batteries to simultaneously achieve high energy and long cycle life.

1. Introduction

All-solid-state lithium batteries (ASSLB) are promising for electric vehicles and large-scale storage systems. Among all the solid electrolytes, sulfide electrolytes attracted extensive attention due to the high ionic conductivity after simply cold-pressing [1-3]. To achieve a high cell-level energy density, the high energy cathodes (FeS_2, S [4, 5] or lithium transition metal oxide ($LiCoO_2$, $LiNi_xCo_yMn_zO_2$ ($x + y + z$ =1)) [6-9]) and Li metal anodes have to be employed, which requires sulfide electrolytes to be stable for both Li and high energy cathodes. Sulfide electrolytes are compatible with the sulfide cathode [10] and $LiNbO_3$-coated lithium transition metal oxide cathodes. However, the sulfide electrolytes are unstable to metallic lithium, and cannot form a robust solid electrolyte interphase (SEI). The continuous reaction between sulfide electrolyte and Li anode increases the interface resistance, resulting in fast capacity degradation of the ASSLB. Besides, the uneven Li deposition during Li plating and voids formation during Li stripping also accelerate the lithium dendrite growth in sulfide electrolytes.[11-13] Although the voids can be suppressed by applying a high pressure [14], filling a eutectic Na–K liquid metal [15], or forming a lithiophilic Li-M (M=alloy metal) interlayer [8, 16-18], the critical current density of solid electrolyte is still less than 1.5 mA cm^{-2} at an areal capacity of 3 mAh cm^{-2} [15] because the solid electrolytes are still reduced by Li. Replacement of Li metal with Li-M alloy anodes that have a high lithiation potential (such as Sn and Bi) can suppress the reduction of sulfide electrolytes and maintain sufficient contact at solid electrolyte/anode interface.[19, 20] However, it also reduces the cell voltage and anode capacity, thus lowering the cell energy density. Artificially inserting a lithiophobic interphase or doping sulfide electrolyte with fluorine [21] to *in-situ* form a lithiophobic interphase (such as LiF) between sulfide electrolyte and Li can prevent Li from plating on sulfide electrolyte surface suppressing sulfide electrolyte reduction and Li dendrite growth. However, the low ionic conductivity of LiF interlayer increased the interface resistance. To reduce the interface overpotential but still suppress Li dendrite, we mixed a highly ionic-conductive Li_3N with LiF forming a porous lithiophobic LiF-Li_3N layer between Li and solid electrolyte.[22] The deposited Li can reversibly penetrate into pores of the LiF-Li_3N particle layer without amplifying into dendrite, resulting in a stable overpotential even if Li plating capacity increased due to the increased contact interface between Li and LiF-Li_3N.[22] To further reduce the Li plating/stripping overpotential, Li_3N in LiF-Li_3N was replaced by electronic conductive Li_xMg.[23] LiF-Li_xMg interlayer was *in-situ* formed by dropping $Mg(TFSI)_2$-LiTFSI-DME liquid electrolyte between LGPS and Li followed by a drying process. The dense LiF-Li_xMg interlayer enabled LGPS to achieve a critical current density of 1.3 mA cm^{-2} at a capacity of 1.3 mAh cm^{-2}, similar to or even higher than that of Li_6PS_5Cl.[24] However, the low critical current density limits the energy density of Li metal full cells. Rational designing the interphase inserted between sulfide solid electrolyte and Li using graphite can achieve a high critical current density of 10 mA cm^{-2}, however, the capacity was limited to 0.25 mAh cm^{-2}.[25] Adding Ag@carbon interlayer between Li_6PS_5Cl and current collector enables Li plating on current collector without penetration into carbon interlayer.[8] However, the inherent mechanism for Li plating at C/current collector interface not in Ag@carbon interlayer was still unclear.

To simultaneously suppress Li dendrite growth and reduce the interface resistance even at a high capacity, the interlayer should satisfy several stringent requirements: (1) The interlayer should have a high ionic and moderate electronic conductivity to prevent Li from plating on solid electrolytes but on current collector with a low Li plating/stripping overpotential; (2) The interlayer should be lithiophobic with a porous structure to enable reversible Li penetration/extraction into interlayer pores from the current collector without amplifying into Li dendrite (similar to reversible water penetration/extraction into hydrophobic PTFE pores at varied pressure) even at a high Li plating/stripping capacity; (3) The interlayer on current collector side should be lithiophilic promoting uniform Li plating on the current collector with a low overpotential and ensuring intimate contact between Li and lithiophobic layer. However, the formation of such an interlayer is still challenged and has not been reported yet.

Herein, we *in-situ* constructed a porous lithiophobic-lithiophilic interlayer by inserting a mixed ionic-electronic conductive (MIEC) lithiophobic & porous LiF-C-Li_3N-Bi nano-composite interlayer between Li_6PS_5Cl solid electrolyte and Li anodes (**Figure 1**a). During Li plating, Li penetrates into porous LiF-C-Li_3N-Bi layer and alloy with the Bi nanoparticles forming Li_3Bi alloys (Figure 1b). The lithiophilic Li_3Bi and Li_3N nanoparticles will move along with plated Li toward to current collector, while the high lithiophobic LiF-C still stay in the original site (Figure 1c). The nano-Ag particle migration from the Ag@C interlayer to the current collector was also observed by Samsung's group.[8] The driving force for lithiophilic Li_3Bi-Li_3N (not lithiophobic LiF-C) migration from LiF-C-Li_3N-Li_3Bi interlayer to Li anode is the high lithiophobicity difference between Li_3Bi-Li_3N and LiF-C. In the following Li plating/stripping cycles, Li uniformly deposits on the lithiophilic Li_3Bi-Li_3N layer and reversibly penetrate into/extract from the porous LiF-C sublayer (Figure 1c-d). The highly lithiophobic (a contact angle of 138^o) and high ionic conductive (10^{-5} S cm^{-1}) LiF-C-Li_3N-Bi layer enables Li to only deposit at LiF-C-Li_3N-Bi/Cu interface rather than Li_6PS_5Cl/LiF-C-Li_3N-Bi interface (Figure 1d) suppressing Li_6PS_5Cl reduction and Li dendrite growth. In addition, the low electronic conductivity (3.4×10^{-7} S cm^{-1}) of the LiF-C-Li_3N-Bi layer also further inhibits the reduction of Li_6PS_5Cl solid electrolyte. Moreover, the high ionic conductivity and lithiophilic Li_3Bi-Li_3N sublayer also reduced Li plating/stripping overpotential to 50 mV at a current density of 0.5 mA cm^{-2}. The LiF-C-Li_3N-Bi/LiF-C/Li_3Bi-Li_3N interlayer enabled Li anode to achieve a high CE of 99.6% at 0.2 mA cm^{-2}/0.2 mAh cm^{-2} after 28th cycle and 98.7% at 1.0 mA cm^{-2}/1.0 mAh cm^{-2} after 45th cycle. Besides, $Co_{0.1}Fe_{0.9}S_2$/Li_6PS_5Cl/Li cell with the MIEC lithiophobic-lithiophilic interlayer can stable charge/discharge for 854 cycles at current density of 150 mA g^{-1} at room temperature. The reversible Li penetration/extraction into a mixed conductive & porous lithiophobic/lithiophilic interlayer is fundamental different from Li plating at the interface of current collector/carbon (without Li penetration into carbon) [8] and other reported interlayers.[21, 25-30] The designed porous lithiophobic-lithiophilic interlayer changed the two-dimension planar Li plating/stripping to three-dimensional Li penetration/extraction into/from porous lithiophobic interlayer, which can reduce the stress during Li plating, thus reducing the cell stack pressure. Besides, the lithiophilic Li_3N-Li_3Bi sublayer on Cu current collector guides uniform Li plating/stripping, preventing voids formation between Li metal and the skeleton of the porous lithiophobic layer, thus decreasing the cell overpotential at high rates.

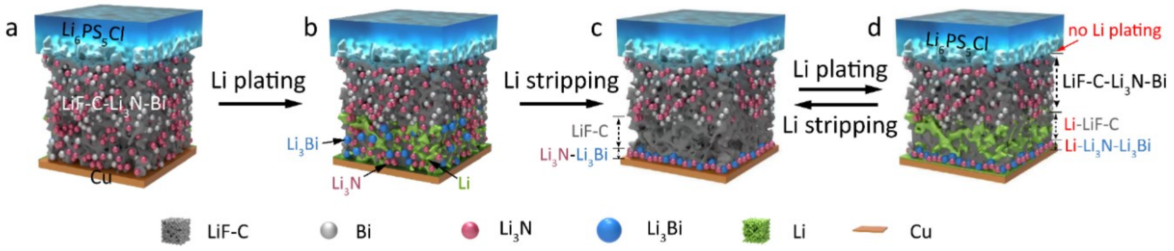

Figure 1. Illustration for the in-situ formation of LiF-C-Li_3N-Bi/LiF-C/Li_3N-Li_3Bi lithiophobic/lithiophilic interlayer during Li plating/stripping process

2. Results and Discussions

2.1. Formation of LiF-C/Li_3Bi-Li_3N lithiophobic/lithiophilic sublayer

LiF-C-Li_3N-Bi nanocomposites were synthesized by ball-milling of BiF_3-CF-Li_3N mixture with designed composition (Figure S1), where the Bi molar ratio in LiF-C-Li_3N-Bi is less than 1.5% to ensure high lithiophobicity. The formation of Li_3Bi on the surface of LiF-C-Li_3N-Bi interlayer contacting with current collector during Li plating was confirmed by X-ray powder diffraction (XRD) characterization (**Figure 2**a). During lithiation of Li/LiF-C-Li_3N-Bi/Li_6PS_5Cl/LiF-C-Li_3N-Bi/SS half-cell to 0.5 mAh cm^{-2} (B point in Figure 2a & Figure S2), characteristic peaks for LiBi at 20.8° and Li_3Bi at 22.9° appears (Figure 2a). Upon further lithiation to Li plating at 1.0 and 1.5 mAh cm^{-2} (C and D points in Figure 2a and Figure S2), LiBi further lithiates into Li_3Bi, and the peak intensity for Bi at ~27° (Figure S1) was significantly reduced compared with that before Li plating (Figure 2a). However, a large amount of Bi still remained as evidenced by the peaks at 38° and 45.8° (Figure 2a). Since the low electronic conductivity (3.4×10^{-7} S cm^{-1}, Figure S3) and the high lithiophobicity (contact angle of 138°, Figure S4) of LiF-C-Li_3N-Bi composite prevent the Li deposition inside the LiF-C-Li_3N-Bi interlayer, only the Bi nanoparticles that contacted with Cu and deposited Li transferred into Li_3Bi alloys, which is also evidenced by the very low capacity of Bi in LiF-C-Li_3N-Bi nanocomposite in the first lithiation process. As shown in Figure S5, the capacity ratio of the first lithiation capacity above 0.0V (0.488 mAh) to the theoretical capacity of Bi to Li_3Bi in LiF-C-Li_3N-Bi nanocomposite (36.477 mAh, see detailed calculation method below Figure S5) is only 1.3%, demonstrating that only 1.3% of Bi nanoparticles that contacted with current collector was converted into Li_3Bi. The high overpotential (204 mV) in the first Li plating in Figure S5 is attributed to the strong lithiophobicity of LiF-C-Li_3N-Bi and high stress.[31] In the following Li plating/stripping cycles, the Li_3Bi nanoparticles stay on current collector.[32] Apart from the migration of Li_3Bi, near-surface Li_3N nanoparticles also move to the current collector during Li plating, which will be discussed in the next section.

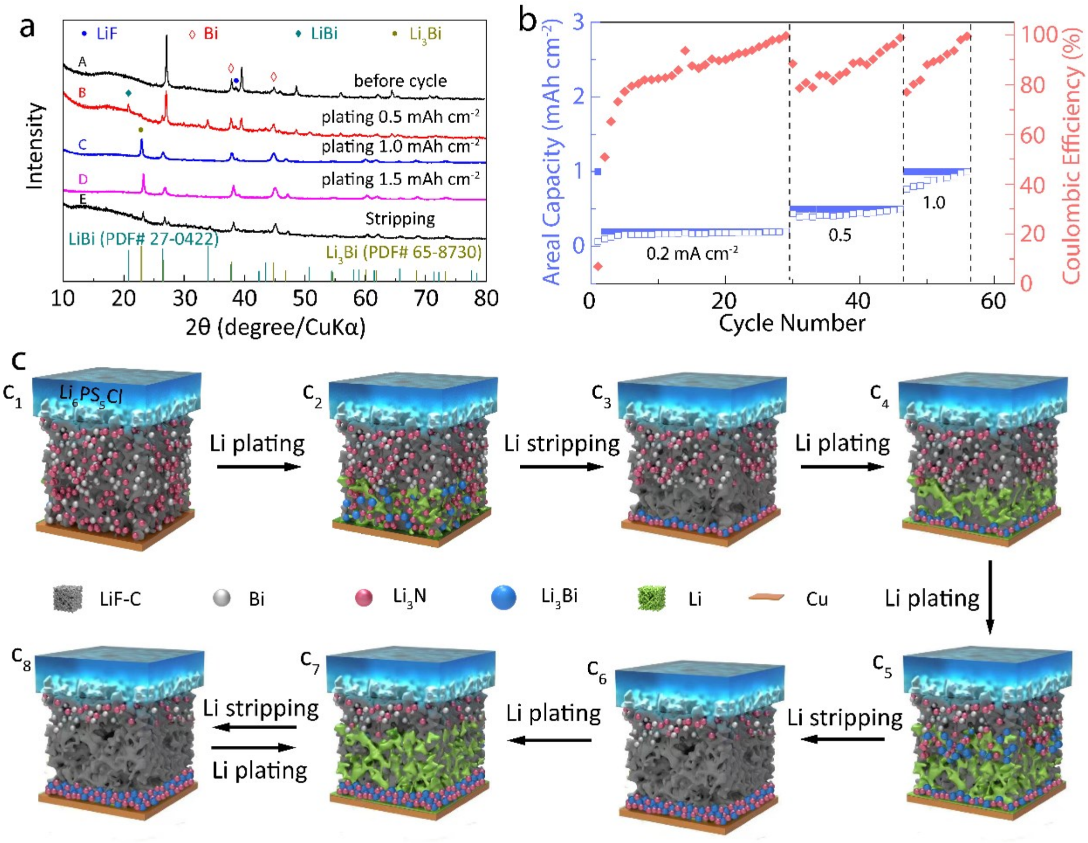

Figure 2. XRD and CE tests for Li/LiF-C-Li_3N-Bi/Li_6PS_5Cl/LiF-C-Li_3N-Bi/SS half-cell. (a) XRD patterns of LiF-C-Li_3N-Bi layer in Li/LiF-C-Li_3N-Bi/Li_6PS_5Cl/LiF-C-Li_3N-Bi/SS half-cell during first Li plating and stripping cycle after removing SS (SS=stainless steel current collector). (b) Li plating/stripping CE of Li/LiF-C-Li_3N-Bi/Li_6PS_5Cl/LiF-C-Li_3N-Bi/SS half-cell at different current densities and capacities under room temperature and stack pressure of 1.0 MPa. (c) Illustration of Li plating/stripping process at LiF-C-Li_3N-Bi/Cu interface.

Due to the low electronic conductivity of LiF-C-Li_3N-Bi (3.4×10^{-7} S cm^{-1}; Figure S3) and high lithiophobicity of carbon, the carbon is also inactive to Li in LiF-C-Li_3N-Bi nanocomposite, which is confirmed by Raman spectra of LiF-C-Li_3N-Bi after Li plating. As shown in Figure S6, after Li plating, the

Raman shift of carbon is the same as the pristine one, demonstrating lithium was not inserted into carbon.[33, 34] Besides, the intensity of D band is much higher than that of G band, indicating the electronic conductivity of carbon in the interlayer is low, which can suppress the reduction of Li_6PS_5Cl electrolyte.

The Li deposition overpotential gradually decreased with Li plating/stripping cycles (Figure S7). Since deposited Li can penetrate into LiF-C-Li_3N-Bi interlayer, the contact area between Li and LiF-C-Li_3N-Bi increases with capacity (Figure 2c), resulting in a low ASR of 50 $\Omega\cdot cm^2$ (Figure S7) at 0.5 mA cm^{-2}/0.5 mAh cm^{-2}. The Li plating overpotential is almost independent with capacity due to increased contact area at a high Li plating capacity, which is unique for the LiF-C-Li_3N-Bi interlayer. The fabrication of thick (50 µm, Figure S8) LiF-C-Li_3N-Bi interlayer is to ensure no Li plating on the Li_6PS_5Cl electrolyte surface even at a high capacity. After activation cycles, Li plating/stripping CE at step-increased capacity was evaluated using Li/LiF-C-Li_3N-Bi/Li_6PS_5Cl/LiF-C-Li_3N-Bi/CC half-cell at a cut-off voltage of 0.5 V to avoid the lithiation/delithiation of Li_3Bi and decomposition of Li_3N. The Li plating/stripping CE reached 99.6% at 0.2 mA cm^{-2}/0.2 mAh cm^{-2} after 28th cycle, 99.4% at 0.5 mA cm^{-2}/0.5 mAh cm^{-2} after 45th cycle and 98.7% at 1.0 mA cm^{-2}/1.0 mAh cm^{-2} after 55th cycle (Figure 2b). The gradually increased CE with Li plating/stripping cycles at each capacity was caused by the gradual conversion of Bi to Li_3Bi when deposited Li penetrated into the pores of LiF-C-Li_3N-Bi interphase (Figure 2c_1-c_2). After the formed Li_3Bi moved along with Li to current collector during Li plating, small amount of unreacted Bi will further react with plated Li in following Li plating, and repeat the process until all the Bi particles in LiF-C-Li_3N-Bi interlayer that contact with the deposited Li are converted to Li_3Bi (Figure 2c_{3-4}), CE will reach a stable value. When the capacity and current density are further increased, the CE drops again and then gradually increases. This is because more Li will penetrate into porous LiF-C-Li_3N-Bi with an increased Li plating capacity (Figure 2c_5), which converts additional Bi in LiF-C-Li_3N-Bi into Li_3Bi, resulting in the CE drops again. However, the CE will increase with Li plating/stripping cycles at a fixed capacity. Eventually, the CE will reach a stable value again (Figure 2c_7-c_8). The low CE due to the irreversible conversion of Bi to Li_3Bi in the first few cycles can be mitigated by pre-cycle at low current density to a required capacity (activation cycles). As shown in Figure S9, after activation cycles at a low current density of 0.5 mA cm^{-2} to a high capacity of 1.5 mAh cm^{-2}, Li/LiF-C-Li_3N-Bi/Li_6PS_5Cl/LiF-C-Li_3N-Bi/Cu cell reached a high CE of 98.2% at 0.5 mA cm^{-2}/0.5 mAh cm^{-2} since the Bi has been lithiated to Li_3Bi in the pre-cycles. CE of 98.2% at 0.5 mA cm^{-2}/0.5 mAh cm^{-2} after pre-cycles is significantly higher than that (88%) when the capacity step-increased from 0.2 mA cm^{-2}/0.2 mAh cm^{-2} to 0.5mA cm^{-2}/0.5 mAh cm^{-2} (Figure 2b). In sharp contrast, the CE of Li/Li_6PS_5Cl/SS cell can only reach 81.8% (Figure S10) due to the reduction of Li_6PS_5Cl by Li.

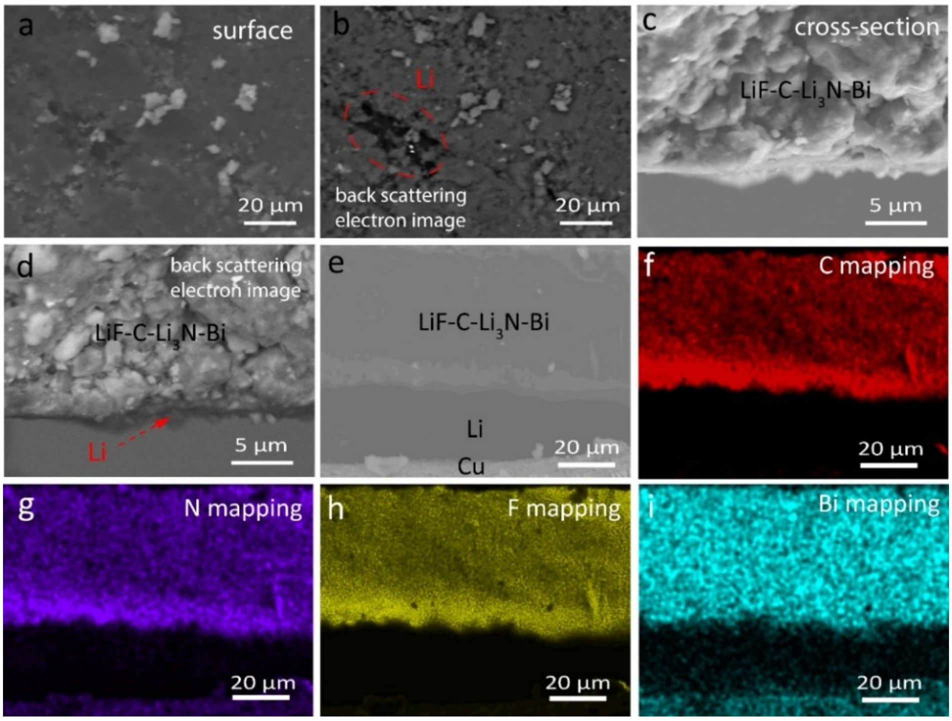

Figure 3. Morphology and elements distribution of LiF-C-Li_3N-Bi layer during Li plating/stripping. (a) SEM images and (b) backscattering electron images for the surface of LiF-C-Li_3N-Bi layer after 10th Li plating. (c) Cross-section SEM images and (d) backscattering electron images of LiF-C-Li_3N-Bi layer after Li plating. (e) Cross-section SEM image of Li_6PS_5Cl/LiF-C-Li_3N-Bi/Li layers after Li plating. EDS images of element (f) C, (g) N, (h) F and (i) Bi at Li_6PS_5Cl/LiF-C-Li_3N-Bi/Li layers after Li plating (The EDS image for Cu current collector can be found in Figure S11).

The migration of lithiophilic nanoparticles from LiF-C-Li_3N-Bi interlayer to current collector during Li plating/stripping was investigated using scanning electron microscope (SEM) images. As shown in Figure S8, the cycled LiF-C-Li_3N-Bi interlayer (Figure S8b) remains similar thickness as pristine cell (Figure S8a) since only the Bi nanoparticles at the near-interface of current collector/LiF-C-Li_3N-Bi reacted with deposited Li. Before cycling, the particles on the surface of LiF-C-Li_3N-Bi layer are closely contacted with each other (Figure S8c). After Li plating to 1.5 mAh cm^{-2}, the surface of LiF-C-Li_3N-Bi layer becomes rough (Figure S8d) due to the volume expansion of surface-layer Bi during alloying reaction. Furthermore, from the SEM and backscattering electron image (**Figure 3**a-b, Figure S8d-e), the deposited Li metal can be observed on the surface of LiF-C-Li_3N-Bi layer contacting to current collector. Besides, the obviously intensive O distribution (Figure S8b and S12, O mapping) and backscattering electron image (Figure 3b and 3d) at LiF-C-Li_3N-Bi/SS interface after the Li plating proved that Li only deposited on the current collector. While, for Li_6PS_5Cl/CC interface without LiF-C-Li_3N-Bi interlayer, Li penetrated into the Li_6PS_5Cl electrolyte during Li plating (Figure S13), which will reduce the electrolyte and promote lithium dendrite growth. After Li stripping, dead lithium remains at the Li_6PS_5Cl/CC interface (Figure S14). In sharp contrast, Li was fully stripped from the LiF-C-Li_3N-Bi/SS interface (Figure S12d-f), proving the high Li plating/stripping reversibility at the LiF-C-Li_3N-Bi/SS interface.

To preserve the morphology of LiF-C-Li_3N-Bi/Li interface during cell disassembling, SS current collector in Li/LiF-C-Li_3N-Bi/Li_6PS_5Cl/LiF-C-Li_3N-Bi/SS cell was replaced by soft Cu foil. Then, the cross-section SEM images were collected at LiF-C-Li_3N-Bi/LiCu interface after Li plating. As shown in Figure 3, the lithiophilic Li_3Bi (Figure 3i, Bi mapping) and Li_3N (Figure 3g, N mapping) nanoparticles moved to Cu current collector (below deposited Li) after Li plating/stripping cycles. The migration of lithiophilic Li_3Bi and Li_3N from LiF-C-Li_3N-Bi sublayer to current collector during Li plating will also lead to the increased intensity for C (Figure 3f) and F (Figure 3h) in LiF-C-Li_3N-Bi near to Li. Besides, the intimate interface contact between LiF-C-Li_3N-Bi and Li is well maintained after continuous cycling (Figure 3e), which can decrease the interface overpotential and prevent the high local current density.

The migration of Li_3N and Li_3Bi from LiF-C-Li_3N-Li_3Bi to the current collector during Li plating/stripping cycles was further confirmed by ToF-SIMS. Figures S15a and S15c show the crater sputtered by a Ga$^+$ ion beam for the LiF-C-Li_3N-Bi layer before cycling. As shown in **Figure 4**a and Figure S16a, elements Li, F and N before Li plating/stripping cycles are homogeneously distributed in LiF-C-Li_3N-Bi interlayer. After 10th Li plating, Li and N content on the surface of LiF-C-Li_3N-Bi (contacting to current collector) become very high and then rapid decrease along the depth of LiF-C-Li_3N-Bi and finally get back to the normal content when reaching to bulk LiF-C-Li_3N-Bi layer (Figure 4b and Figure

S16b). The V-shape Li distribution is attributed to the migration of Li_3N and Li_3Bi from LiF-C-Li_3N-Li_3Bi to current collector, which increases the surface Li content but reduces the Li content in the remained LiF-C. Since the Li density of Li_3Bi-Li_3N is higher than Li, the migration of Li_3Bi-Li_3N towards current collector during Li plating/stripping will lead to high lithium content on the surface forming Li_3N-Li_3Bi/Li-LiF-C/LiF-C-Li_3N-Bi structure after Li plating, forming V shape of Li distribution and the continuously increased F content along depth and level-off to the F content in the bulk LiF-C-Li_3N-Bi layer (Figure 4b). The formation of Li_3Bi-Li_3N/LiF-C/LiF-C-Li_3N-Bi lithiophilic/lithiophobic structure significantly suppressed the Li dendrite growth and reduced interface resistance during Li plating.

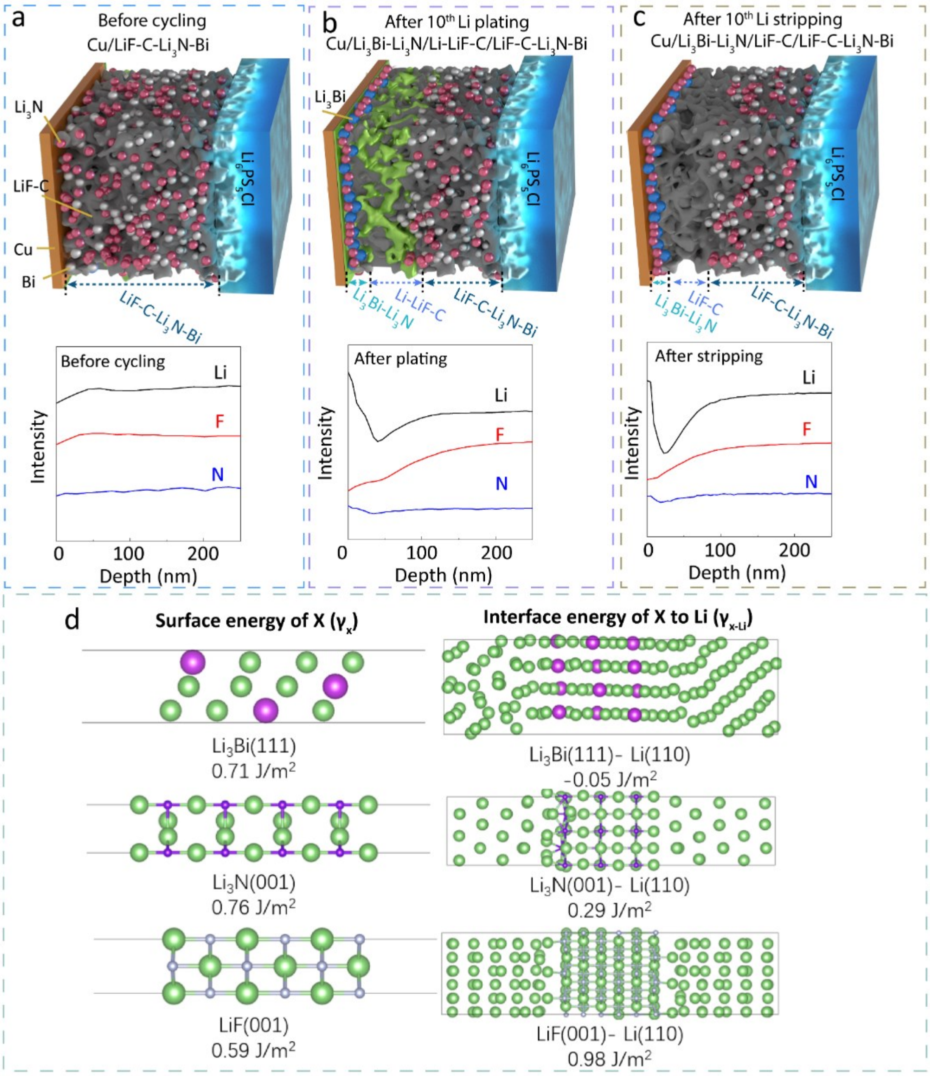

Figure 4. Illustration, characterization and simulations on interface evolution from lithiophobic LiF-C-Li_3N-Bi to lithiophilic/lithiophobic gradient Li_3N-Li_3Bi/Li-C/LiF-C-Li_3N-Bi during Li plating/stripping. F and N distribution at LiF-C-Li_3N-Bi/SS interlayer (a) before cycling, after (b) Li plating and (c) Li stripping (the full Li, F and N distribution curves along the depth of the sputtered crater were shown in Figure S14). (d) Atomic structures, surface energy and interface energy of Li_3Bi surface, Li_3N surface, LiF surface, Li_3Bi-Li, Li_3N-Li and LiF-Li and interface.

After Li stripping (Figure S17 shows the Ga^+ ion beam sputtered crater), CC/Li_3N-Li_3Bi/Li-LiF-C/LiF-C-Li_3N-Bi changed to CC/Li_3N-Li_3Bi/LiF-C/LiF-C-Li_3N-Bi, and lithiophilic/lithiophobic nature is still maintained, as demonstrated by similar but narrowed V shape of Li and N distribution and leaner increase in the interlayer after Li stripping (Figure 4c and Figure S16c). Since deposited Li has been stripped, only possibility for the high Li content at LiF-C-Li_3N-Bi/CC interface is the migrated Li_3Bi-Li_3N particles remaining on the surface of current collector after Li stripping (to 0.5 V), as proved by the high N and Li content on Li_3Bi-Li_3N/LiF-C-Li_3N-Bi surface after Li stripping (Figure 4c and Figure S16c). The stripping of Li also induces a rapid F increase in Li_3Bi-Li_3N/LiF-C/LiF-C-Li_3N-Bi composition (Figure 4c). The irreversible Li_3N and Li_3Bi migration to current collector after Li plating can also be observed in the mapping of Li (Figure S15b) and F (Figure S15d) along the depth of Li_3Bi-Li_3N/LiF-C/LiF-C-Li_3N-Bi. The *in-situ* formation of a stable Li_3Bi-Li_3N/LiF-C/LiF-C-Li_3N-Bi lithiophilic/lithiophobic interlayer after Li plating/stripping cycles enables Li to uniform deposit on lithiophilic Li_3Bi-Li_3N surface, while the lithiophobic LiF-C/LiF-C-Li_3N-Bi layer can prevent the deposited Li from contacting Li_6PS_5Cl electrolyte avoiding the reduction of Li_6PS_5Cl (Figure S18-19). The lithiophobic LiF-C/LiF-C-Li_3N-Bi layer can also suppress the lithium dendrite growth, thus improving the Li plating/stripping CE.

The mechanism for the irreversible migration of Li_3N and Li_3Bi during Li plating and stripping was analyzed using DFT calculation. The thermodynamic distribution of a material X in Li is governed by its interface energy of X and Li. A lithiophobic material shows a higher concentration on the surface of Li, while a lithiophilic material shows a higher concentration on the bulk of Li. Therefore, lithiophilic materials near the interface are then infiltrated into Li bulk during Li plating due to strong attractive bonding, while the lithiophobic materials will then stay on the original site due to a strong repel force. After the first few Li plating/stripping processes, lithiophilic materials will irreversibly migrate to the current collector surface and serve as nucleation sites in the bottom for subsequent Li plating. As lithiophobic materials are pushed off by the Li, the surface lithiophobic materials will stay on the top surface of plated Li. The lithiophilic-lithiophobic property of materials X to Li is determined by Young's equation.

$$\cos\theta = \frac{\gamma_x - \gamma_{x-Li}}{\gamma_{Li}} = \frac{\Delta\gamma}{\gamma_{Li}} \qquad (1)$$

ϑ is the contact angle between Li and substrate material X, γ_x is surface energy of X, $\gamma_{x\text{-Li}}$ is the interface energy of X to Li, γ_{Li} (0.61 J m^{-2}) is the surface energy of Li, $\Delta\gamma = \gamma_x - \gamma_{x\text{-Li}}$. When $0^o<\vartheta<90^o$, X is lithiophilic to Li, which means Δγ value is positive, and the materials with larger Δγ value is more lithiophilic to Li. When $90^o<\vartheta<180^o$, X is lithiophobic to Li, which means Δγ value is negative, and the materials with more negative Δγ value is more lithiophobic to Li. As shown in Figure 4d, the Δγ of Li_3Bi, Li_3N and LiF is 0.76, 0.47 and -0.39 J m^{-2}, respectively, proving Li_3Bi and Li_3N is lithiophilic to Li, and LiF is lithiophobic to Li. Obviously, the $\Delta\gamma_{\text{Li3Bi}} > \Delta\gamma_{\text{Li3N}}$, that is the $\cos\vartheta_{\text{ Li3Bi}} > \cos\vartheta_{\text{ Li3N}}$, implying Li_3Bi is more lithiophilic to Li than Li_3N. Besides, Gibbs free energy ΔG value ($\Delta G = \gamma_{x\text{-Li}} - \gamma_x - \gamma_{\text{Li}}$) for Li spreading on Li_3Bi is negative, which means the spontaneous spreading of Li on Li_3Bi. The contact angle ϑ of Li_3N and LiF was calculated using equation (1). The ϑ of 40^o for Li_3N and 130^o for LiF are in good agreement with the reported experimental data.[35, 36]

From the comprehensive characterizations of XRD, SEM, ToF-SIMS and thermodynamic analyzation, we propose the mechanism for *in-situ* formation of lithiophilic-lithiophobic interlayer from lithiophobic LiF-C-Li_3N-Bi interlayer in Li anode free cell (Figure 2c). During the initial Li plating process, when the potential of Cu current collector drops to below 0.7 V, Bi nanoparticles on LiF-C-Li_3N-Bi surface that contacts with current collector will be lithiated into Li_3Bi forming LiF-C-Li_3N-Li_3Bi surface layer, while the Bi inside LiF-C-Li_3N-Bi interlayer is inactive because the LiF-C-Li_3N-Bi interlayer is highly lithiophobic and has a high ionic conductivity (10^{-5} S cm^{-1}) but a low electronic conductivity (3.4×10^{-7} S cm^{-1}). Upon further Li plating below 0.0 V, Li begins to deposit on Cu and then penetrate into porous LiF-C-Li_3N-Bi to further reduce the Bi in LiF-C-Li_3N-Bi into Li_3Bi. The lithiophilic Li_3Bi and Li_3N tend to migrate into the bulk of deposited Li due to strong bonding of Li to Li_3Bi/Li_3N, while the highly lithiophobic LiF and carbon is pushed-off from Li due to high repel-force. In the following Li stripping process, the Li on top of Li_3Bi-Li_3N layer will be stripped and leave Li_3Bi-Li_3N sticking on the current collector surface (Figure 2c$_{2\text{-}3}$) and serves as nucleation sites for subsequent Li plating (Figure

2c$_4$). During the second Li plating, Li will deposit on the lithiophilic Li_3Bi-Li_3N, pushing the highly lithiophobic LiF and carbon away on the top surface of deposited Li forming a Li_3Bi-Li_3N/Li-LiF-C/LiF-C-Li_3N-Bi composite Li anode (Figure 2c$_4$). The complete formation of lithiophilic/lithiophobic Li_3Bi-Li_3N/LiF-C interlayer may take serval charge/discharge cycles, denoted as activation process. Same as Li anode free cell discussed above, adding Li on LiF-C-Li_3N-Bi interlayer also induces the migration of Li_3Bi-Li_3N to the surface of unreacted Li during Li plating/stripping cycles (Figure S20), which can be proved by the SEM and EDS images of LiF-C-Li_3N-Bi/Li interface after 10 Li plating/stripping cycles at 1.0 mA cm^{-2}/1.0 mAh cm^{-2}, where elements Bi and N were observed at bottom Li (Figure S20d-e), while elements C and F were present in the top LiF-C-Li_3N-Bi layer (Figure S20b-c).

2.2 LiF-C-Li_3N-Bi interlayer for Li dendrite suppression

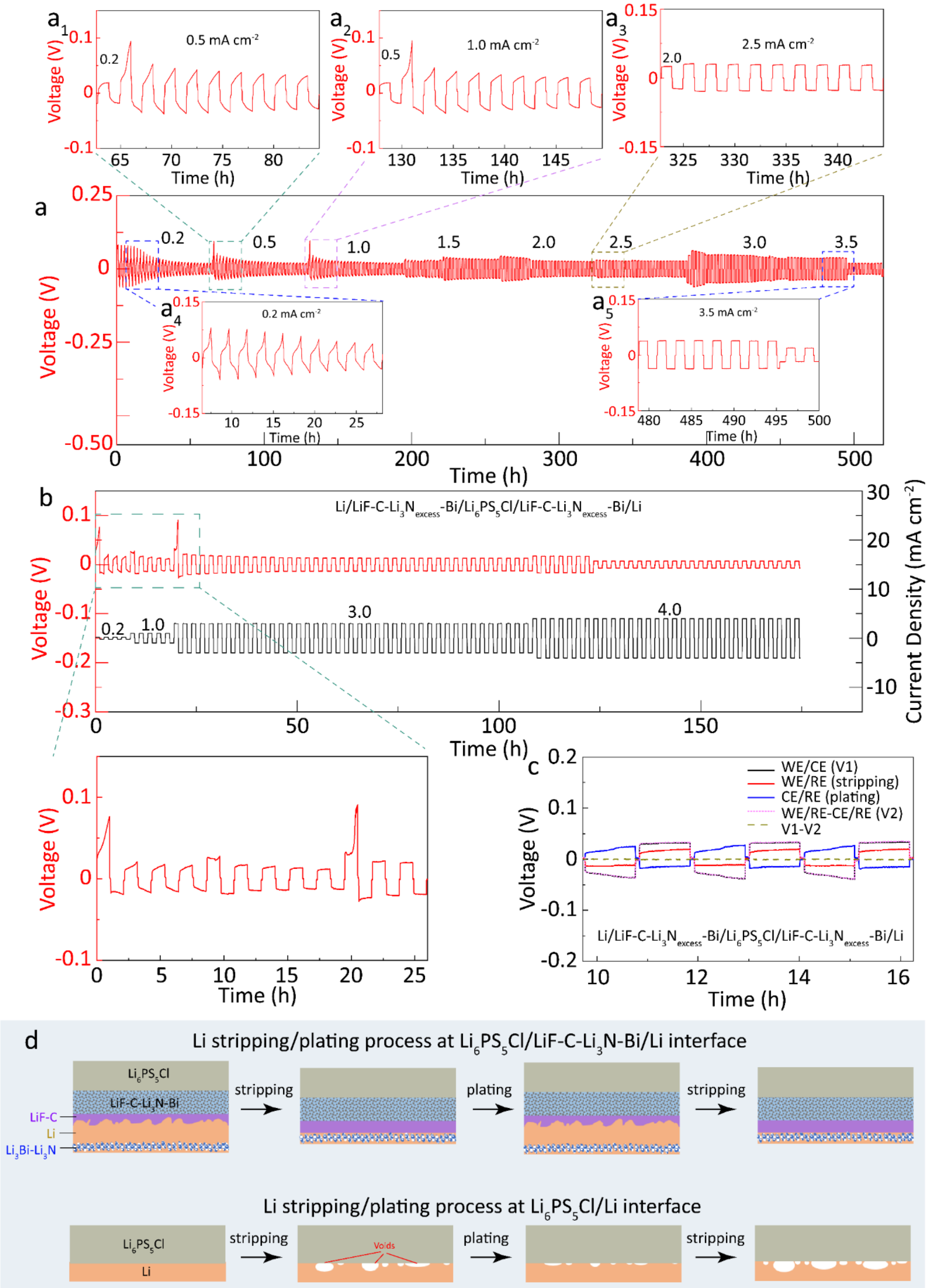
a
a1
0.5 mA cm-2
0.2
a2
1.0 mA cm-2
0.5
a3
2.5 mA cm-2
2.0
a4
0.2 mA cm-2
a5
3.5 mA cm-2
Voltage (V)
Time (h)
0.2
0.5
1.0
1.5
2.0
2.5
3.0
3.5
0.25
0
-0.25
-0.50
0
100
200
300
400
500
b
Li/LiF-C-Li$_3$N$_{excess}$-Bi/Li$_6$PS$_5$Cl/LiF-C-Li$_3$N$_{excess}$-Bi/Li
0.2
1.0
3.0
4.0
Current Density (mA cm^{-2})
30
20
10
0
-10
0.1
0
-0.1
-0.2
-0.3
50
150
c
WE/CE (V1)
WE/RE (stripping)
CE/RE (plating)
WE/RE-CE/RE (V2)
V1-V2
Li/LiF-C-Li$_3$N$_{excess}$-Bi/Li$_6$PS$_5$Cl/LiF-C-Li$_3$N$_{excess}$-Bi/Li
10
12
14
16
d
Li stripping/plating process at Li$_6$PS$_5$Cl/LiF-C-Li$_3$N-Bi/Li interface
Li$_6$PS$_5$Cl
LiF-C-Li$_3$N-Bi
LiF-C
Li
Li$_3$Bi-Li$_3$N
stripping
plating
stripping
Li stripping/plating process at Li$_6$PS$_5$Cl/Li interface
Li$_6$PS$_5$Cl
Li
Voids

Figure 5. Dendrite suppression capability of LiF-C-Li_3N-Bi interlayer. (a) Voltage profile of Li/Li_6PS_5Cl/Li cell with LiF-C-Li_3N-Bi interlayer at a step-increased current density with a fixed charge or discharge time of 1.0 hour under room temperature and stack pressure of 1.0 MPa. (b) Voltage profile of Li/Li_6PS_5Cl/Li cell with LiF-C-Li_3N_{excess}-Bi interlayer at a step-increased current density with a fixed charge or discharge time of 1.0 hour under room temperature and stack pressure of 1.0 MPa. (c) Potential of working electrode (WE) and counter electrode (CE) and the cell voltage of Li/Li_6PS_5Cl/Li with LiF-C-Li_3N_{excess}-Bi interlayer measured in a three-electrode cell. (d) Illustration of Li plating and stripping process at Li_6PS_5Cl/Li interphase with and without LiF-C-Li_3N-Bi interlayer.

The critical current density of Li/Li_6PS_5Cl/Li symmetric cells with and without LiF-C-Li_3N-Bi interlayer was measured at a step-increased current density with a fixed Li plating/stripping time of 1.0 hour. As shown in **Figure 5**a, Li/Li_6PS_5Cl/Li symmetric cell with LiF-C-Li_3N-Bi interlayer experiences activation process in the first few cycles at step-increased current density. The gradual decrease of overpotential in the initial Li plating/stripping cycles in each step-increased current is attributed to the gradually increased contact area between Li and LiF-C-Li_3N-Bi due to more Li penetration into the pores of LiF-C-Li_3N-Bi interlayer, which is also observed in Li plating/stripping profiles of lithiophobic LiF-Li_3N coated Li_3PS_4 electrolyte at a high capacity [22]. The Li penetration into lithiophobic LiF-C-Li_3N-Bi layer increased contact area between Li and LiF-C-Li_3N-Bi, and reduced the impedance (Figure S21). The formation of Li_3Bi-Li_3N/LiF-C/LiF-C-Li_3N-Bi lithiophilic/lithiophobic interlayer enables Li/Li_6PS_5Cl/Li cells to achieve critical current density of > 3.5 mA cm^{-2} at a high capacity of 3.5 mAh cm^{-2} (Figure 5a). However, Li/Li_6PS_5Cl/Li cell without LiF-C-Li_3N-Bi interlayer did not show the activation process and was short-circuit at 0.2 mA cm^{-2}/0.2 mAh cm^{-2} after 28 cycles (Figure S22). Short cycle life of Li/Li_6PS_5Cl/Li cells at room-temperature was also reported in open literatures [24]. Besides, since Li reversibly penetrates/extracts back in the pores of LiF-C-Li_3N-Bi interlayer, the Li plating/stripping voltage is less than 0.15 V even at a high current density of 3.5 mA cm^{-2} and capacity of 3.5 mAh cm^{-2}, which is impossible for traditional Li/Li_6PS_5Cl/Li cell.

Unlike the self-amplified Li dendrite growth in the lithiophilic Li_6PS_5Cl solid electrolyte, the Li penetration into lithiophobic LiF-C/LiF-C-Li_3N-Bi interlayer is a self-limited activation process. The activation process in Li/LiF-C-Li_3N-Bi/Li_6PS_5Cl/LiF-C-Li_3N-Bi/Li cell at a current density of 0.5 mA cm^{-2} and capacity of 0.5 mAh cm^{-2} was investigated using the three-electrode cell with Li reference electrode beside the working electrode (Figure S23a). As shown in Figure S23b-c, the cell voltage (V2, marked by the magenta dot) that is calculated by subtracting potentials of working electrode (WE-RE, marked by the red line) and counter electrode (CE-RE, marked by the blue line) agreed well with the measured cell voltage (V1, marked by the black line), suggesting that the potential of WE and CE during Li stripping and plating were accurately recorded in the configured three-electrode cell. During initial Li plating/stripping of Li/Li_6PS_5Cl/Li cell with LiF-C-Li_3N-Bi interlayer, the potential of both WE (Figure S23d) and CE (Figure S23e) in the first two lithiation is above 0V (*vs.* Li^+/Li RE) due to the lithiation of Bi. As stated early, during Li plating/stripping of Li/Li_6PS_5Cl/Li cells with LiF-C-Li_3N-Bi interlayer, Li first deposits on current collector and then penetrates into porous LiF-C-Li_3N-Bi interlayer to gradually react with the contacted Bi in the LiF-C-Li_3N-Bi sublayer forming Li_3Bi, which requires few activation cycles. During activation cycles, the potential of electrode may be above 0.0V. The required activation cycle numbers decrease with increasing of ionic and electronic conductivity, the capacity of Li plating/stripping in each cycle. After activation cycles, the capacity above 0.0V is much smaller than Li plating/stripping capacity (2% at 1.0 mA cm^{-2}/1.0 mAh cm^{-2} in Figure S7). After forming lithiophilic/lithiophobic Li_3Bi-Li_3N/LiF-C/LiF-C-Li_3N-Bi, the potentials of WE (Figure S23d) and CE (Figure S23e) gradually reduced and became symmetric due to the reduced cell impedances, as evidenced by the decreasing of ionic conduction resistance after 10 cycles in three-electrode cells (Figure S24). The increase of ionic conductivity of the LiF-C-Li_3N-Bi layer by adding Li_3N from 9.5wt% (1.0×10^{-5} S cm^{-1}, Figure S25) to 30.7 wt% can eliminate the activation process (Figure 5b-c and Figure S26), which also further reduce the Li plating/stripping overpotential. In contrast, a quite asymmetric with a much larger and steeper potential in Li stripping than that in Li plating was observed in Li/Li_6PS_5Cl/Li cells without LiF-C-Li_3N-Bi interface layer due to voids formation in Li stripping and partial void-heal in Li plating[13] (Figure S27). Since the voids formed in Li stripping is only partially healed in the followed Li plating process, the voids will continuously grow during repeat Li stripping/plating cycles, resulting in the decreased contact between Li and Li_6PS_5Cl electrolyte (Figure 5d), eventually leading to short-circuit of Li/Li_6PS_5Cl/Li cell. In contrast, for Li/Li_6PS_5Cl/Li cells with LiF-C-Li_3N-Bi interlayer, the potential difference between plating and stripping is highly reversible during cycling (Figure S23c) because the deposited Li can reversibly penetrate/extract in/from lithiophobic LiF-C sublayer, which ensures good interface contact between Li and electrolyte (Figure 5d), enabling Li/Li_6PS_5Cl/Li cell to stable cycle even at a high current density. The *in-situ* formed MIEC lithiophilic/lithiophobic Li_3Bi-Li_3N/LiF-C/LiF-C-Li_3N-

Bi interlayer overcome two critical challenges of Li dendrite growth and high interface resistance by (1) preventing the formation of voids at Li/SSE through reversible Li penetration/extraction; (2) avoiding the reduction of SSE through plating Li at the interface of Cu/interlayer rather than on SSE surface; (3) suppressing uncontrolled Li dendrite growth through a strong lithiophobic LiF-C sublayer; (4) reducing the overpotential through uniformly deposition of Li on lithiophilic sublayer on Cu surface and reversible penetration/extraction of Li in MIEC LiF-C-Li_3N-Bi interlayer. The multifunctional role of lithiophobic/lithiophilic MIEC interlayer has been demonstrated by significantly increasing the critical current density of Li/Li_6PS_5Cl/Li cell from 0.4 mA cm^{-2} (Figure S28) to 3.5 mA cm^{-2} and a high CE of 99.6% for Li/Li_6PS_5Cl/CC half-cell after 28th cycles at 0.2 mA cm^{-2}/0.2 mAh cm^{-2}. The critical current density of Li_6PS_5Cl can be further enhanced by increasing the ionic conductivity of LiF-C-Li_3N-Bi interlayer through increasing the Li_3N weight ratio, as demonstrated by the short circuit of the symmetric cell at a higher current density of 4.0 mA cm^{-2} at high capacity of 4.0 mAh cm^{-2} (Figure 5b). Besides, the Li plating overpotential in Li/LiF-C-Li_3N_{excess}-Bi/Li_6PS_5Cl/LiF-C-Li_3N_{excess}-Bi/SS cell also decreased to 10 mV at the 10th cycle (Figure S29). This work also highlights the importance of interfacial ionic conductivity on lithium dendrite suppression capability, and its effect on cell performance will be explored in detail in our following work.

The lithiophilic/lithiophobic interlayer for Li dendrite suppression is universal for solid electrolytes, especially for those solid electrolytes that are not stable with Li. As shown in Figure S30, the LiF-C-Li_3N-Bi interlayer also enables Li_3PS_4-LiI electrolyte to stably charge/discharge at a high current density of 3.0 mA cm^{-2} with a high capacity of 3.0 mAh cm^{-2} in room temperature, which is three times higher than the critical current density of the Li_3PS_4-LiI without lithiophilic/lithiophobic interlayer reported by us [12]. In addition, the lithiophilic Bi in LiF-C-Li_3N-Bi can be replaced by lithiophilic Ag. The Li dendrite suppression capability of LiF-C-Li_3N-Ag was evaluated using Li_3PS_4-LiI electrolyte. LiF-C-Li_3N-Ag composite was synthesized using the same procedures as LiF-C-Li_3N-Bi composite. As shown in Figure S31, the Li/LiF-C-Li_3N-Ag/Li_3PS_4-LiI/LiF-C-Li_3N-Ag/Li symmetric cell can also stably charge/discharge at a high current density of 2.0 mA cm^{-2} with a high capacity of 2.0 mAh cm^{-2} in room temperature. The effective lithiophilic-lithiophobic interlayer for Li dendrite suppression does not have to be *in-situ* formed from mix-conductive lithiophobic interlayer, the artificial lithiophilic-lithiophobic interlayer can also suppress Li dendrite. As shown in Figure S32, the artificial lithiophobic/lithiophilic LiF-C-Li_3N/LiSr interlayer enables Li_6PS_5Cl electrolyte to charge/discharge at a high current density of 2.0 mA cm^{-2} with a high capacity of 2.0 mAh cm^{-2} at room temperature.

2.3 Performance of all-solid-state battery employing the mix conductive interlayer

The impact of LiF-C-Li_3N-Bi layer on the electrochemical performance of all-solid-state batteries was investigated using $Co_{0.1}Fe_{0.9}S_2$ cathodes and excess Li anode. Because $Co_{0.1}Fe_{0.9}S_2$ has good compatibility to sulfide electrolyte, the impact of the side reaction between cathode material and electrolyte on the full cell performance can be excluded. As shown in **Figure 6**, the $Co_{0.1}Fe_{0.9}S_2$/Li_6PS_5Cl/LiF-C-Li_3N-Bi/Li battery shows a long cycle life of 854 cycles at a current density of 150 mA g^{-1}. When $LiCoO_2$ (LCO) was used as the cathode material, the LCO/Li_3YCl_6/Li_6PS_5Cl/LiF-C-Li_3N-Bi/Li cell can also stable cycle up to 50 cycles (Figure S33). When increasing the weight ratio of Li_3N in the LiF-C-Li_3N-Bi interlayer, LiF-C-Li_3N_{excess}-Bi interlayer enables the LCO/Li_3YCl_6/Li_6PS_5Cl/LiF-C-Li_3N_{excess}-Bi/Li cell to stable cycle up to 100 cycles at cathode loading of 1.0 mAh cm^{-2} (Figure S34), proving the superior lithium dendrite suppression capability of LiF-C-Li_3N-Bi-based interlayer.

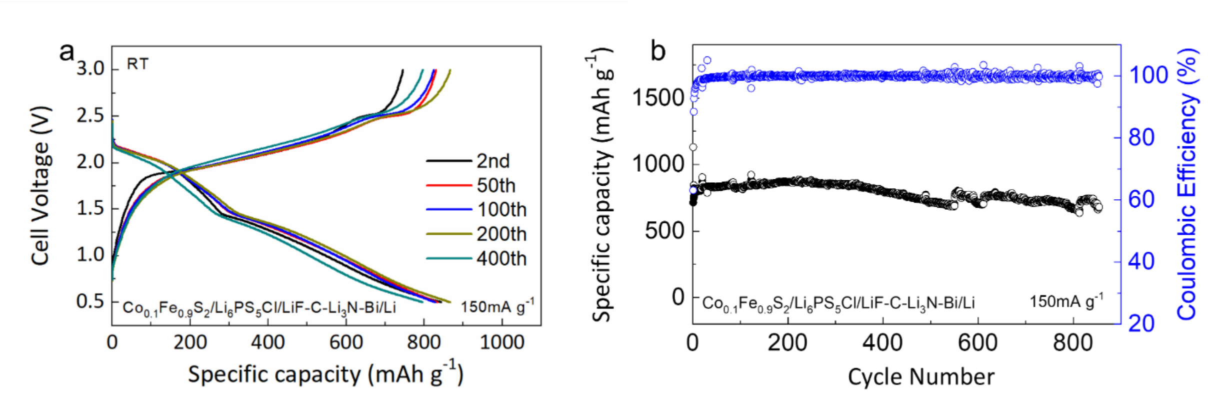

Figure 6. Performance of all-solid-state lithium battery with LiF-C-Li_3N-Bi interlayer. (a) Galvanostatic charge/discharge curves and (b) Cyclic performance of $Co_{0.1}Fe_{0.9}S_2$/Li_6PS_5Cl/LiF-C-Li_3N-Bi/Li cell with cathode loading of 1.4 mAh cm^{-2} (the mass loading of $Co_{0.1}Fe_{0.9}S_2$ active material was 1.6 mg cm^{-2}). All the tests were performed at room temperature and stack pressure of 2.5 MPa.

To understand the origin of the excellent cycling stability of $Co_{0.1}Fe_{0.9}S_2$/Li_6PS_5Cl/LiF-C-Li_3N-Bi/Li cells, the potential of $Co_{0.1}Fe_{0.9}S_2$ cathode and Li anode and cell voltage during charge/discharge was monitored using the three-electrode battery (Figure S35). The capacity and CE of

$Co_{0.1}Fe_{0.9}S_2/Li_6PS_5Cl/Li$ cell (Figure S35a) reduced in the second cycles, while the capacity and CE of $Co_{0.1}Fe_{0.9}S_2/Li_6PS_5Cl/LiF-C-Li_3N-Bi/Li$ cell increase in the second cycles (Figure S35b). The decay in capacity and CE in $Li/Li_6PS_5Cl/Li$ is mainly attributed to the instability between Li_6PS_5Cl and Li anode, as evidenced by the reduced Li anode capacity in the second cycles (Figure S35c). The Li anode in $Co_{0.1}Fe_{0.9}S_2/Li_6PS_5Cl/LiF-C-Li_3N-Bi/Li$ cell has a very low overpotential in the second cycles (Figure S35d). A lower capacity of $Co_{0.1}Fe_{0.9}S_2/Li_6PS_5Cl/LiF-C-Li_3N-Bi/Li$ cell than that of $Co_{0.1}Fe_{0.9}S_2/Li_6PS_5Cl/Li$ battery in the first cycle (Figure S35a-b) is attributed to high impedance of pristine $LiF-C-Li_3N-Bi$ interlayer. After the first activation process, $Co_{0.1}Fe_{0.9}S_2/Li_6PS_5Cl/LiF-C-Li_3N-Bi/Li$ cell shows much reversible charge/discharge behavior than $Co_{0.1}Fe_{0.9}S_2/Li_6PS_5Cl/Li$ cell in the second cycle (Figure S35e-f), further proving the effectiveness of lithiophobic/lithiophilic $LiF-C-Li_3N-Bi/LiF-C/Li_3Bi-Li_3N$ interlayer for guiding Li to uniformly deposit under the bottom Li. Compared with the reported researches, our work presented here has the advantages of high current density and high capacity at room temperature that is desired for industry application (Table S1). Besides, the universality of the interlayer design principle reported in this work can extend to other solid-state metal batteries.

3. Conclusion

In summary, Li dendrite growth and high interface impedance are two critical challenges for all-solid-state Li batteries. We mitigate both challenges by introducing a mixed ionic/electronic conductive (MIEC) lithiophobic $LiF-C-Li_3N-Bi$ interlayer between Li_6PS_5Cl electrolyte and Li anode to avoid Li plating on Li_6PS_5Cl electrolyte surface. The lithiophobic $LiF-C-Li_3N-Bi$ interlayer partially converts into lithiophobic/lithiophilic $LiF-C/Li_3Bi-Li_3N$ on the Li side after few plating/stripping cycles. The lithiophilic Li_3Bi-Li_3N layer enables uniform lithium deposition, while highly lithiophobic porous LiF-C enables reversible Li penetration/extraction during Li plating/stripping without forming Li dendrite due to the high interface energy. The formed lithiophilic/lithiophobic interface enables the $Li/Li_6PS_5Cl/Li$ symmetric cell to stable cycle at a high current density of 3.0 mA cm^{-2} at high capacity of 3.0 mAh cm^{-2}, and $Li/Li_6PS_5Cl/CC$ half-cell to achieve CE of 99.6% at 0.2 mA cm^{-2}/0.2 mAh cm^{-2}. Furthermore, all-solid-state lithium batteries employing $Co_{0.1}Fe_{0.9}S_2$ cathode material both show excellent cycling stability. This work provides a universal strategy to design high-performance all-solid-state battery.

Supporting Information

Supporting Information is available from the Wiley Online Library or from the author.

Acknowledgements

This work was supported by the US Department of Energy (DOE) under Award number DEEE0008856 and ARPA-E under Award of DE-AR0000781. H. Wan and B. Zhang contributed equally to this work

Received: ((will be filled in by the editorial staff))
Revised: ((will be filled in by the editorial staff))
Published online: ((will be filled in by the editorial staff))

References

1. Kato, Y., Hori, S., Saito, T., Suzuki, K., Hirayama, M., Mitsui, A., Yonemura, M., Iba, H. ,Kanno, R., *Nat. Energy* **2016**, *1*, 16030.
2. Gao, Z., Sun, H., Fu, L., Ye, F., Zhang, Y., Luo, W. ,Huang, Y., *Adv. Mater.* **2018**, *30*, 1705702.
3. Bachman, J.C., Muy, S., Grimaud, A., Chang, H.H., Pour, N., Lux, S.F., Paschos, O., Maglia, F., Lupart, S., Lamp, P., Giordano, L. ,Shao-Horn, Y., *Chem. Rev.* **2016**, *116*, 140-162.
4. Wan, H., Liu, G., Li, Y., Weng, W., Mwizerwa, J.P., Tian, Z., Chen, L. ,Yao, X., *ACS Nano* **2019**, *13*, 9551-9560.
5. Zhou, L., Assoud, A., Zhang, Q., Wu, X. ,Nazar, L.F., *J. Am. Chem. Soc.* **2019**, *141*, 19002-19013.
6. Deng, S., Sun, Q., Li, M., Adair, K., Yu, C., Li, J., Li, W., Fu, J., Li, X., Li, R., Hu, Y., Chen, N., Huang, H., Zhang, L., Zhao, S., Lu, S. ,Sun, X., *Energy Storage Mater.* **2021**, *35*, 661-668.

7. Li, X., Ren, Z., Norouzi Banis, M., Deng, S., Zhao, Y., Sun, Q., Wang, C., Yang, X., Li, W., Liang, J., Li, X., Sun, Y., Adair, K., Li, R., Hu, Y., Sham, T.-K., Huang, H., Zhang, L., Lu, S., Luo, J. ,Sun, X., *ACS Energy Lett.* **2019**, *4*, 2480-2488.

8. Lee, Y.-G., Fujiki, S., Jung, C., Suzuki, N., Yashiro, N., Omoda, R., Ko, D.-S., Shiratsuchi, T., Sugimoto, T., Ryu, S., Ku, J.H., Watanabe, T., Park, Y., Aihara, Y., Im, D. ,Han, I.T., *Nat. Energy* **2020**, *5*, 299-308.

9. Kim, D.H., Oh, D.Y., Park, K.H., Choi, Y.E., Nam, Y.J., Lee, H.A., Lee, S.M. ,Jung, Y.S., *Nano Lett.* **2017**, *17*, 3013-3020.

10. Yao, X.Y., Liu, D., Wang, C.S., Long, P., Peng, G., Hu, Y.-S., Li, H., Chen, L.Q. ,Xu, X.X., *Nano Lett.* **2016**, *16*, 7148-7154.

11. Shen, Y., Zhang, Y., Han, S., Wang, J., Peng, Z. ,Chen, L., *Joule* **2018**, *2*, 1674-1689.

12. Han, F., Yue, J., Zhu, X. ,Wang, C., *Adv. Energy Mater.* **2018**, *8*, 1703644.

13. Kasemchainan, J., Zekoll, S., Jolly, D.S., Ning, Z., Hartley, G.O., Marrow, J. ,Bruce, P.G., *Nat. Mater.* **2019**, *18*, 1105.

14. Wang, M.J., Choudhury, R. ,Sakamoto, J., *Joule* **2019**, *3*, 2165-2178.

15. Park, R.J.Y., Eschler, C.M., Fincher, C.D., Badel, A.F., Guan, P., Pharr, M., Sheldon, B.W., Carter, W.C., Viswanathan, V. ,Chiang, Y.-M., *Nat. Energy* **2021**, *6*, 314-322.

16. Krauskopf, T., Mogwitz, B., Rosenbach, C., Zeier, W.G. ,Janek, J., *Adv. Energy Mater.* **2019**, *9*, 1902568.

17. Yang, C., Xie, H., Ping, W., Fu, K., Liu, B., Rao, J., Dai, J., Wang, C., Pastel, G. ,Hu, L., *Adv. Mater.* **2019**, *31*, e1804815.

18. Fan, X., Ji, X., Han, F., Yue, J., Chen, J., Chen, L., Deng, T., Jiang, J. ,Wang, C., *Sci. Adv.* **2018**, *4*, eaau9245.

19. Sakuma, M., Suzuki, K., Hirayama, M. ,Kanno, R., *Solid State Ionics* **2016**, *285*, 101-105.

20. Han, S.Y., Lee, C., Lewis, J.A., Yeh, D., Liu, Y., Lee, H.-W. ,McDowell, M.T., *Joule* **2021**, *5*, 2450-2465.

21. Zhao, F., Sun, Q., Yu, C., Zhang, S., Adair, K., Wang, S., Liu, Y., Zhao, Y., Liang, J., Wang, C., Li, X., Li, X., Xia, W., Li, R., Huang, H., Zhang, L., Zhao, S., Lu, S. ,Sun, X., *ACS Energy Lett.* **2020**, *5*, 1035-1043.

22. Ji, X., Hou, S., Wang, P., He, X., Piao, N., Chen, J., Fan, X. ,Wang, C., *Adv. Mater.* **2020**, *32*, 2002741.

23. Wan, H., Liu, S., Deng, T., Xu, J., Zhang, J., He, X., Ji, X., Yao, X. ,Wang, C., *ACS Energy Lett.* **2021**, *6*, 862-868.

24. Liu, G., Weng, W., Zhang, Z., Wu, L., Yang, J. ,Yao, X., *Nano Lett.* **2020**, *20*, 6660-6665.

25. Su, Y., Ye, L., Fitzhugh, W., Wang, Y., Gil-Gonza, E. ,Li, X., *Energy Environ. Sci.* **2020**, *13*, 908.

26. Niu, S., Zhang, S.-W., Li, D., Wang, X., Chen, X., Shi, R., Shen, N., Jin, M., Zhang, X., Lian, Q., Huang, R., Amini, A., Zhao, Y. ,Cheng, C., *Chem. Eng. J.* **2022**, *429*, 132156.

27. Cheng, Y., Ke, X., Chen, Y., Huang, X., Shi, Z. ,Guo, Z., *Nano Energy* **2019**, *63*, 103854.

28. Kim, S.Y. ,Li, J., *Energy Mater. Adv.* **2021**, *2021*, 1519569.

29. He, X., Ji, X., Zhang, B., Rodrigo, N.D., Hou, S., Gaskell, K., Deng, T., Wan, H., Liu, S., Xu, J., Nan, B., Lucht, B.L. ,Wang, C., *ACS Energy Lett.* **2021**, *7*, 131-139.

30. Zhang, H., Liao, X., Guan, Y., Xiang, Y., Li, M., Zhang, W., Zhu, X., Ming, H., Lu, L., Qiu, J., Huang, Y., Cao, G., Yang, Y., Mai, L., Zhao, Y. ,Zhang, H., *Nat. Commun.* **2018**, *9*, 3729.

31. Yan, K., Lu, Z., Lee, H.-W., Xiong, F., Hsu, P.-C., Li, Y., Zhao, J., Chu, S. ,Cui, Y., *Nat. Energy* **2016**, *1*, 16010.

32. Chen, J., Li, Q., Pollard, T.P., Fan, X., Borodin, O. ,Wang, C., *Mater. Today* **2020**, *39*, 118-126.

33. Gu, Z., Liang, F., Chen, Z., Sadana, A., Kittrell, C., Billups, W.E., Hauge, R.H. ,Smalley, R.E., *Chem. Phys. Lett.* **2005**, *410*, 467-470.

34. Maurin, G., Bousquet, C., Henn, F., Bernier, P., Almairac, R. ,Simon, B., *Solid State Ionics* **2000**, *136-137*, 1295.

35. Krat, S.A., Popkov, A.S., Gasparyan, Y.M., Pisarev, A.A., Fiflis, P., Szott, M., Christenson, M., Kalathiparambil, K. ,Ruzic, D.N., *Fusion Eng. Des.* **2017**, *117*, 199-203.

36. Wang, J., Wang, H., Xie, J., Yang, A., Pei, A., Wu, C.-L., Shi, F., Liu, Y., Lin, D., Gong, Y. ,Cui, Y., *Energy Storage Mater.* **2018**, *14*, 345-350.

All-solid-state lithium batteries with high Li plating/stripping Coulombic efficiency and high critical current density can be achieved by in-situ formation of LiF-C/Li_3N-Li_3Bi lithiophobic/lithiophilic gradient layer at Li/Li_6PS_5Cl interface through the migration of lithiophilic Li_3Bi and Li_3N nanoparticles from LiF-C-Li_3N-Li_3Bi sub-interlayer to the current collector. The lithiophobic/lithiophilic gradient layer enables symmetric cells and full cells to achieve high lithium dendrite suppression capability.

Hongli Wan, Bao Zhang, Sufu Liu, Zeyi Wang, Jijian Xu, Chunsheng Wang*

Interface Design for High-Performance All-Solid-State Lithium Batteries

ToC figure

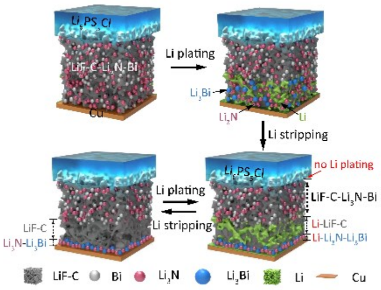
Li_6PS_5Cl
LiF-C-Li_3N-Bi
Cu
Li plating
Li_3Bi
Li_3N
Li
Li stripping
no Li plating
Li_6PS_5Cl
LiF-C-Li_3N-Bi
Li-LiF-C
Li-Li_3N-Li_3Bi
Li plating
Li stripping
LiF-C
Li_3N-Li_3Bi
LiF-C
Bi
Li_3N
Li_3Bi
Li
Cu